Article:
Noor, F and Wen, D (2015) Experimental study of thermal oxidation of nanoscale alloys of aluminium and zinc (nAlZn). Journal of Physics and Chemistry of Solids, 85. pp. 188-196. ISSN 0022-3697

https://doi.org/10.1016/j.jpcs.2015.05.004

Experimental study of thermal oxidation of nanoscale alloys of aluminium and zinc (nAlZn)

Fahad Noor[a] and Dongsheng Wen[b*]

[a]Department of Mechanical Engineering, University of Engineering & Technology, Pakistan

[c] Institute of Particle Science and Engineering, School of Chemical and Process Engineering, University of Leeds, LS2 9JT UK.

[*]E-mail: d.wen@leeds.ac.uk and Tel: 0044 113 3431299

Abstract

Aluminium-based alloys have wide applications but little is known about the thermal-chemical kinetics of nanoalloys. This work investigated the thermal oxidation of Zn and Al nanoalloys (nAlZn) with a BET equivalent diameter of 141 nm through the simultaneous TGA/DSC method. The thermal analysis was combined with elemental, morphology and crystalline structure analysis to elucidate the reaction mechanisms. It was found that the complete oxidation of nAlZn in air can be characterised by a three-stage process, including two endothermic and three exothermic reactions. With the help of ex-situ XRD, different reaction pathways were proposed for different stages, forming the end products of ZnO and $ZnAl_2O_4$. The reactivity comparison between Al and nAlZn suggested that different criteria should be used for different applications.

Keywords: Nanostructures, alloys, thermogravimetric analysis (TGA), thermodynamic properties

1. Introduction

Metallic particles such as aluminium and zinc have important applications in many industries, and alloying is usually used at the bulk scale to improve the material performance. Due to the synergistic effects of the constituent alloying materials, the physicochemical properties of the alloys can be improved by chemical reordering and spatial redistribution of the atoms [1]. In addition, the alloying increases the surface area of the particles that increases the rate of reaction [2, 3]. Aluminium-zinc (AlZn) alloys are good materials for thermal spraying, soldering, and corrosion inhibitors [4, 5], where careful control of the heating is required to either inhibit or to accelerate the oxidation process.

The oxidation mechanism of bulk metals has been well understood, which is diffusion-controlled and the oxide film grows depending on the diffusion coefficients of the reacting species [6, 7]. At the nanoscale, however as the particle size becomes smaller or comparable to the mean free path of air molecules, some deviations from the conventional laws are expected. For instance, the oxidation process may change from the diffusion-controlled to the kinetically-controlled mode [8]. At the nanoscale, it also becomes possible to engineer different properties by controlling the particle structures and morphologies to suit different applications. The oxidation characteristics of individual components of AlZn alloy particles have been widely investigated in the past decade [8-10]. For aluminium nanoparticles, several theories including the diffusion oxidation mechanism (DOM) and melt dispersion mechanism (MDM) have been proposed. At low heating rates, the oxidation process could be described by a shrink-core model, which proceeded as four stages as the temperature increases, controlled by the distinctive phase transition of the oxide and the melting process

[11]. The oxidation process of Zn particles under various environments has also been studied by a few authors. For instance, Aida et al. [10] and Delalu et al.[12] showed that the isothermal oxidation of Zn obeyed the parabolic growth law for micrometer-sized particles. Zhou et al. [13] and Alivov et al. [14] observed that the heating temperature and duration did not change the oxidation process of Zn but influenced the final crystalline structure of ZnO. At the nanoscale, Ma and Zachariah [15] reported two reaction regimes for Zn nanoparticles (50-100 nm), i.e., a slower reaction regime at lower temperatures and a faster oxidation regime occurring at higher temperatures. The oxidation process was suggested to be still diffusion-controlled that could be described by the shrink core model. The reactivity was observed to increase with the decrease of particle size, i.e. the oxidation onset temperature was 250 ^{o}C for 50 nm and ~300 ^{o}C for 100 nm particles.

Some studies have shown that aluminium nanoparticles (nAl) in combination with copper possessed some excellent properties with many potential applications in resistance welding electrodes, electrical connectors, and the metastable intermolecular composites (MICs) [16-19]. It is expected that aluminium – zinc nanoalloys (nAlZn) could also possess some unique thermal-physical properties, which however has no published studies. Their properties in relation to the bulk behaviour and individual elements are still unclear. In this work, a detailed oxidation study of AlZn nanoalloy (nAlZn) was conducted in a simultaneous thermal analysis (TGA/DSC) under a heating rate range of 2 – 30 K/min. The morphology and the crystalline structure of the nAlZn before and after oxidation were characterised with scanning electron microscope (SEM), transmission electron microscope (TEM), and X-ray diffraction (XRD). The oxidation mechanism of nAlZn was elucidated through the close

linkage of the TGA/DSC study with the morphology, elemental and crystalline structure characterizations.

2. Experimental Procedure

The nanoalloy was fabricated by the electrical explosion of wires method (EEW) where the constitutional elements were twisted in wires. The aluminium content in the explosion products was adjusted by varying the wire diameter. The particles were produced in the Tomsk State University, Russia, and stored in vacuum-sealed packs. The details of the process were discussed in refs. [20-22]. The particles produced by this method typically have a wide range of size distribution (PSD) but with low level of contamination [23]. The gas adsorption method, Brunauer–Emmett–Teller (BET) method, was used to determine the surface area of the particles (Gemini VII 2390p Surface Area Analyser, Micromeritics Instruments Corp) by using nitrogen gas as the adsorbent . The sample was degassed using a Gemini FlowPrep degasser at 200 ^{o}C and 10^{-2} Pa for 3 hours before the experiment and the nitrogen adsorption was measured from a five-point isotherm in a relative pressure range of 0.05 to 0.3 at -196 ^{o}C.

The morphology of the particles before and after experiments was observed with scanning electron microscope (SEM) (Inspect F, FEI Company, EU) operating at 10 kV, and a high resolution transmission electron microscopy, HRTEM, (JEOL JEM 2010) operating at 200 kV. The samples were sputter-coated with gold to enhance their electrical conductivity. This type of coating was desired to prevent the specimen from charging the electron beam and to improve the signal-to-noise ratio. The chemical composition of the sample was measured by

Energy Dispersive X-ray Spectroscope (EDXS, Oxford Instruments) equipped with INCA Energy 300 systems.

The oxidation kinetics and physical transitions of the particles during the heating were studied by simultaneous thermal analysis (STA 1500 thermal analyser, Rheometric Scientific, Germany). The temperature calibration of the thermobalance was checked against the melting point standards of metals like Sn, Zn and Pb. 6 ± 0.1 mg of the sample was used for the Thermogravimetric analysis (TGA) and differential Calorimetric analysis (DSC). The particles were oxidized in the temperature range of 25-1200 ^{o}C under iso-thermal and iso-conversion conditions, **Table 1**. Platinum crucibles were used for the experimentation and were cleaned with 10% HNO_3 solution after the completion of each set of experiment. Particles were oxidized under the ambient conditions in dry air maintaining a flow rate of 23 ± 2 ml min^{-1}. The products were cooled in the atmosphere of nitrogen for ex-situ XRD and EM analysis. Parameters that may affect the TGA/DSC experimental results (i.e. reaction gas environment, crucible material and mass of the sample) were kept the same for each set of experimentations, similar to our previous studies [24-27].

The crystalline structure of the nAlZn before and after the heat treatment was examined with ex-situ XRD. The diffractograms were obtained using the conventional XRD with a Siemens (D5000) diffraction meter operated at 40 kV and 40 mA using CuKα radiation ($\lambda = 0.154187$ nm). The diffraction patterns from 10-75^{o} 2θ were recorded for the identification of end products of the experiments.

3. Results and discussions

3.1. Powder characterisation

The morphology of the nAlZn at various temperature conditions was evaluated with SEM. The SEM image of the particles before the oxidation is presented in the **Fig. 1(a)**. Particles have spherical shapes and a soft agglomeration can be observed. The chemical composition of nAlZn was estimated with the Energy-dispersive X-ray spectroscopy (EDS). It was found that the sample contained 4.8% of oxygen, 18.3% of Al and 76.9 % of Zn, i.e., in the molar ration of 1:2.25:3.91 for O, Al, and Zn respectively. The EDS spectrum showed a weak signal of oxygen, **Fig. 1(b).** The diffractogram of the particles did not show any peak of the oxide compound. This suggests that the oxide contained by the particles was in the amorphous phase. However it is unclear about the exact form of the oxides, i.e. ZnO, Al_2O_3 or some other compounds. The active meal content enclosed inside the oxide layer could be in the regime of 80%~94% of the metal content. With the help of TEM, it was found that the particles were blanketed by a passivation layer having a thickness of ~5-6 nm. The TEM image shows that the diameter of the particle ranged from 28 to 240 nm, **Fig. 2**.

X-ray diffraction (XRD) of the sample shown in **Fig. 3** revealed that the nAlZn was in the solid solution form. No peaks of any intermetallic compounds of Zn and Al, which should be formed with definite stoichiometric ratios, were observed. The XRD pattern showed the peaks of aluminium (JCPDS No. 04-0787) at $2\theta = 38.52^{o}$, 44.80^{o}, 65.21^{o} and of zinc (JCPDS No. 04-0831) at $2\theta = 36.31^{o}$, 39.0^{o}, 43.26^{o}, 54.33^{o}, 70.09^{o}, 70.66^{o}. No peaks of any other material were observed, which means that the sample was in the pure form. The BET surface area of the sample particle was determined as 7.73 m^2/g. Assuming that all

particles having smooth spherical shapes, the BET equivalent diameter d_{BET} was calculated with the relationship $A_{BET} = 6/ (\rho * d_{BET})$ [27], where A_{BET} is the specific area, ρ is the density of the particles (taken as 5.5 g/cc) and d_{BET} is the equivalent diameter of the particles. The calculated equivalent diameter was 141 nm, which is in the range of TEM observation.

3.2. Thermal Chemical Characteristics

The samples were oxidised in the atmosphere of dry air by the simultaneous TGA/DSC system. The oxidation characteristics of n-AlZn were similar under all heating rates investigated. The heating rate of 10 K/min was taken as an example to illustrate the thermal behaviour and oxidation kinetics of nAlZn from 25 to 1200 ^{o}C, **Fig. 4**. According to variation of the energy and sample mass, the whole process can be generally divided into three stages with the increase of the temperature. The first stage started from the room temperature (RT) and ended at 390 ^{o}C, the second stage was from 390 to 725 ^{o}C, and the third stage started at 725 ^{o}C and extended to the completion of heat treatment process at 1200 ^{o}C. These three stages are explained separately below.

3.2.1. Stage one (RT- 390 ^{o}C)

During this temperature range, two endothermic reactions were observed in the DSC curve. The first peak was observed at 285 ^{o}C and the second peak was emerged at 382 ^{o}C. In this zone no weight gain was observed on the TGA curve. This suggests that both endothermic reactions were related to the physical changes occurring in the particles. It is believed that the first endothermic peak was related to the phase transition of the alloy and the second one was due to the eutectic melting, which are explained below.

It is known that Zn and Al metals do not make intermetallic compounds due to the weak interaction between their atoms, but Zn is soluble in Al [28] , which is also shown by the XRD result, **Fig. 2**. The solubility of zinc in the aluminium increases with the increase of the temperature. AlZn is characterised with two phases of alloy as shown in the phase diagram, **Fig. 5**. The first one is face centred cubic (fcc) structured, which is the α–phase (contains ~1% Zn, ~99% Al), and the second is a hexagonal close packed (hcp) structured, the β–phase (contains ~ 99% Zn, ~ 1% Al). Both phases of AlZn alloy slowly but gradually reach the equilibrium state. The capacity to attain the equilibrium increases with the increase of temperature. When the temperature reaches 285 ^{o}C, there is a transformation of β-phase (hcp) → α–phase (fcc) [29, 30]. This transformation is an endothermic process and is believed to be associated with the first endothermic peak of DSC curve at 285 ^{o}C. To examine whether this phase transformation is reversible or not, a separate experiment was performed, where the particles were heated to 400 ^{o}C at the heating rate of 10 K/min and then cooled to the RT in the atmosphere of nitrogen, under the same heating rate, **Fig. 6**. During the heating process, the particles went through a phase transformation, associated with a peak emerged ~ 287 ^{o}C. On the cooling run, the reverse transition from α (fcc) → β (hcp) was observed near 240 ^{o}C, which is 47 K below the transition temperature, showing the temperature hysteresis.

The second peak at 382 ^{o}C is identified as the eutectic melting of the AlZn alloy. The phase diagram of AlZn alloy, **Fig. 5,** shows the important transformation points at 277 ^{o}C, 381 ^{o}C, 420 ^{o}C and 660 ^{o}C. Point (a), which shows the transformation of phases, is at 277 ^{o}C in the phase diagram, appears at 285 ^{o}C in the DSC curve. This upward shift of temperature is believed to be associated with the reduction of particle size to the nanometer scale. Point (b)

is the eutectic melting temperature of the alloy. There is no difference of eutectic melting point, ~382 ^{o}C, of the alloy in its bulk and nanometer scales. The points (c) and (d) represent the melting temperatures of Zn and Al, respectively.

3.2.2. Stage two (390 ^{o}C - 725 ^{o}C)

Stage 2 is the first exothermic zone that characterised with various interesting points. On the TGA curve, this zone starts from point 'a' and ends at point 'b'. During this step of oxidation, a total weight change of 21.2 % was observed and two exothermic peaks were emerged shown in the DSC curve. The DSC curve deviated for the first time at ~430 ^{o}C, showing the start of the oxidation reaction. The first peak attained the maxima at 604 ^{o}C and ended at 635 ^{o}C. The second peak emerged at 635 ^{o}C, reached the maxima at 652 ^{o}C and ended at 725 ^{o}C. During the first peak, 13 % weight of the sample was increased. To understand the path of the oxidation, two separate experiments were performed where the samples were heated from the RT to 625 ^{o}C and 710 ^{o}C respectively, under the same heating rate. The products were cooled in the atmosphere of nitrogen gas and XRD and EDS analysis were performed. The XRD traces of the products are given in **Fig. 7** (d) and (e). The peaks of ZnO (JCPDS card no. 36-1451) were emerged at 625 ^{o}C which shows the oxidation of zinc. XRD also showed the weak peaks of γ-alumina (JCPDS card No. 10-0425), which can be attributed to the combined effect of reaction of aluminum with oxygen and the transformation of amorphous alumina. As also suggested by the EDS and TEM, the particles were covered with a passivation layer of amorphous oxide. Consequently, the chemical reactions taking place in the temperature range of 430~635 ^{o}C are proposed as,

$$2Zn + O_2 \rightarrow 2ZnO \qquad (1)$$

$2Al + 3/2O_2 \rightarrow \gamma\text{-}Al_2O_3$ (2)

$\text{Amorphous-}Al_2O_3 \rightarrow \gamma\text{-}Al_2O_3$ (3)

The XRD trace of the products at 710 ^oC shows the intensities of ZnO peak was increased whereas the intensities of Zn and Al peaks were decreased. Weak peaks of $ZnAl_2O_4$ (JCPDS card No. 05-0669) also emerged at this temperature. Peaks of ZnO and Zn overlaped at $2\theta = 36.3^o$. The reaction pathways in the temperature range of 635~ 725^o C were therfore proposed as the combination of reactions (1), (2) and (4) below:

$ZnO + \gamma\text{-}Al_2O_3 \rightarrow ZnAl_2O_4$ (4)

The second stage was characterised with two interesting peaks, particularly the second one. In order to interpret both peaks and their relationship with the physical state of Al, the sample was heated from room temperature to 700 ^oC in the environment of nitrogen under a heating rate of 10 K/min, **Fig. 8.** It is interesting to note that the endothermic peak of the DSC in nitrogen environment coincided with the rise of the exothermic peak in the air. Consequently this showed that first peak happens when some part of the Al was in the solid state and Zn was in the liquid state. The second peak occurred after the melting of the remaining Al in the alloy. Due to the increased mobility of Al in its molten state, the reaction between Al, oxygen and ZnO was accelerated that ultimately forms $ZnAl_2O_4$, as shown in **Fig. 7** (d) and (e). Due to this 'synergic reaction' the span of the reaction was increased and more heat was produced. It is shown from the phase diagram, **Fig. 5**, that all the alloy was transformed into a molten state at point (d), 660 ^oC. For nAlZn used in this work, the full melting was observed at 652

^{o}C, which was due to the nano size effect of the particles. After attaining the 2nd peak, the rate of the reaction decreased once again, and 8.2% weight was increased during this sub-step.

3.2.3. Stage three (725 ^{o}C-1200 ^{o}C)

Stage 3 was the 2nd exothermic zone where the rate of oxidation was increased from 725 ^{o}C and peaked at 817 ^{o}C. After attaining the peak, the rate of the reaction decreased till it reached 1200 ^{o}C where the experiment ended. During this stage, 7.2 % of the weight of sample was increased. The TGA curve became flat at 1045 ^{o}C, which suggests that the reaction was complete. Similarly two additional experiments were conducted by heating the samples from room temperature to 910 ^{o}C and 1200 ^{o}C respectively, at β =10 K/min in order to identify the crystalline structure and elemental information. XRD showed that the peaks of Zn and Al were weakening at T~ 910 ^{o}C, **Fig. 7** (f) and (g). Different to the oxidation of pure nAl where the phase transition, i.e. forming various polymorphs of alumina (γ-, δ-, θ-, and α-Al_2O_3) as the temperature increase, was dominant [25], we did not observe any other forms of the alumina for nAlZn, probably due to the small portion of the Al atoms in the alloy. The peak of γ-Al_2O_3 can not be observed at the 3rd stage **,** which suggests that the alumina was reacting with ZnO forming $ZnAl_2O_4$. As the temperature increased, the peaks of ZnO and $ZnAl_2O_4$ were getting stronger. Consequently the proposed reaction pathways remained the same as Eqs. 1, 2 and 4. After reaching 817 ^{o}C, the rate of reaction decreased. The TGA signal became flat at point 'c' in the TGA-DSC curve, i.e., 1045 ^{o}C, which shows that the reaction was complete and all nAlZn were consumed. The end products were ZnO and $ZnAl_2O_4$. As shown in **Fig.** 10, the final weight gain after the full oxidation changed slightly at different heating rates. If taking an average final weight increase ~29%, the molar

ratio of ZnO to $ZnAl_2O_4$ can be estimated as ~5:1 accordingly. This is consistent qualitatively with the XRD result, Fig. 7f. The increase of the $ZnAl_2O_4$ ratio in the 1200 ^oC temperatue might be associated with the effect of the evaporation of part zinc at high temperature and continuous convertion of ZnO.

During the oxidation process, the morphology of the particles changed at different temperatures, **Fig.** 9. The particles retained their spherical shapes while went through various oxidation steps, **Fig**. 9 (a), (b) and (c). Significant morphological changes were observed at higher temperature ~ 1200 ^oC where some particles were agglomerated into big structures of multigonal crystals and needle-like fibrous structures, **Fig**. 9 (d), (e) and (f). This type of morphology was not observed for the oxidation of pure aluminium nanoparticles under similar experimental conditions, which can be attributed to the diffusion of Zn ions occurring in some preferential directions [31]. High temperature (~1200 ^oC) promoted the migration of grain boundaries and merged the small grains transforming them into the large ones. The elemental composition analyses (EDS) shows that the ratio of metallic (Al+Zn) to the oxygen atom decreased as the temperature increases, reaching the final ratio of 2.86 at 1100 ^oC, **Table 2**.

3.3. Effect of heating rate

The TGA and DSC profiles under the entire heating rate, from 2 to 30 K/min, are given in **Fig. 10**. It shows clearly that the scenario described above is applicable to all the other heating rates. The whole oxidation process can be still described by a three-stage scenario but with slight change of the temperature boundaries for different stages. The key features of oxidation at different heating rates are summarized in **Table 3-5**. **Table 3** shows the

characteristics of the endothermic reactions, such as the characteristic temperature and enthalpy change; **Table 4** shows the mass changed during various oxidation steps, and **Table 5** summarizes the exothermic reactions including the temperature and heat flow. As descrbied earlier, the endothermic peaks were due to the phase transition and the eutectic melting. The mass changed during the first oxidation zone was found to decrease slightly with the increase of the heating rate. For instance at heating rate of 2 K/min its value was 21.6 %, which decreased to 20.1% at 30 K/min. Contrary to that, the mass increased during the second oxidation zone was proportional to the heating rate, e.g., its value was 3.72% at the heating rate of 5 K/min and increased to 6.4% at 30 K/min. The total mass gained during the whole oxidation process decreased slightly with the increase of the heating rate. The mean value of the mass gained during the whole oxidation process was 28.7 ± 0.5 %.

The XRD traces of nAlZn oxidized from room temperature to 1200 ^{o}C under various heating rates (5, 10 and 20 K/min) are shown in **Fig. 11**. Similar elements and composition are shown regardless of the heating rate. The major end products of the oxidisation were ZnO and $ZnAl_2O_4$. Again no peaks of Al and Zn were observed, which suggests that all the specimen were oxidized.

The enthalpy analysis of different stages of oxidation at different heating rates, **Fig. 12**, shows clearly that the energy produced during first and the second exothermic reactions (i.e, 2^{nd} and 3^{rd} stage) differed greatly from each other. For example, the heat produced during the first reaction was 4837 J/g at 10 K/min that constituted 88.5 % of the total energy produced. On the other hand, its value for the second reaction was 630 J/g, which was only 11.5 % of the total energy produced. The total mass changed during the whole reaction was 26.6 %, out of which 21.4 % of mass increase was observed during the first reaction and only 5.5 % of

the mass was changed in the second exothermic reaction. Clearly the energy produced during a specific oxidation step depended upon the metal content available for the reaction. During the first reaction, Zn was in the molten form whereas the complete melting of Al occured after 635 ^{o}C, which increased the rate of the oxidation process. This in turn increased the span of the reaction, resulting in more energy produced. During the second exothermic reaction, only a small amount of sample's mass was left. The total heat released of nAlZn was in the range of 4.5~7 kJ/g considering all the heating rates, which is consistent with thermodynamic values of the bulk materials.

The specific heat released ($\Delta H_{ox}/\Delta m$, rel. units) analysis is taken as the ratio of the area under the DSC curve (thermal effect of oxidation) to the corresponding mass changed (on the TGA curve) [32]. This implies the relative thermal effect, i.e. the ability of energy release. **Fig. 12** (b) shows the values of specific heat produced during the first, second stage of the exothermic and the whole oxidation process. The values were similar for all stages with a weak dependence on the heating rate.

Conventionally, the particle reactivity is described by its metal content, which is however not sufficient to quantify the reactivity for nanoparticles. Not only the metal content, the reactivity of nanoparticles depends upon also the particles size and distribution, the thickness and physicochemical characteristics of the passivation layers, and powder synthesis techniques. It is possible that the particles having similar metal content and/or similar diameters but behave differently in the oxidative environment. Four parameters, namely, the onset temperature (T_{on}), the temperature at which the maximum oxidation rate is achieved (T_{01}), the degree of oxidation (α) up to a certain temperature, and the specific heat release

(ΔH/Δm), have been proposed to compare the reactivity of different nanoparticles [32, 33]. Table 6 shows an example of the comparison between nAlZn and nAl with an average particle size of ~210 nm. As these values are insensitive to the heating rate, the numbers are averaged with a standard deviation reflecting the difference among the heating rates. Clearly nAl has a particle size ~1/3 larger than that of nAlZn, which has some disadvantages in the comparison. If neglecting the particle size effect for the time being, Table 6 shows that nAlZn is more reactive if considering the onset oxidation temperature, and the degree of oxidation at the end of the major, i.e, the first exothermic reaction. UP to 73.1% was converted for nAlZn at 730^{o}C, whereas only 43.5% is observed for nAl, which is related to the smaller oxidation temperature of the zinc. However the temperature to reach the maximum oxidation rate is higher, and the specific heat effect is slightly smaller for nAlZn, which implies that nAl is more reactive. It appears that different parameters should be used for different applications. For instance for applications considering the low temperature effect, the conversion ratio and onset temperature criterion should be used, whereas for applications focusing on the thermal effect, the relative specific heat effect should be used.

4. Conclusions

This paper studied the thermal oxidation of Zn and Al nanoalloys (nAlZn) having a BET equivalent diameter of 141 nm by the simultaneous TGA/DSC method. The thermal analysis was combined with elemental, morphology and crystalline structure analysis to elucidate the reaction mechanisms. It can be concluded that:

- The complete oxidation of nAlZn in air can be characterised by a three-stage scenario, including two endothermic and three exothermic processes.

- The first stage occurred between room temperature and ~ 400 ^{o}C, includes two endothermic reactions, which was due to the phase transformation and the eutectic melting.
- The second stage extended to ~750 ^{o}C, involving the first and the second exothermic reactions, where the 2nd peak is associated with the melting of Al component.
- The third stage included the third exothermic peak until the completion of the reaction at ~ 1050 ^{o}C, and was associated with the conversion of the formed alumina to $ZnAl_2O_4$.
- The reaction pathways forming intermediate products of ZnO and γ-Al_2O_3 were proposed with the help of ex-situ XRD, leading to the end products of ZnO and $ZnAl_2O_4$.
- The comparison of nanoparticle reactivity suggested that different criteria should be used for different applications.

Acknowledgement

This work was financially supported by the Program for Professor of Special Appointment (Eastern Scholar) at Shanghai Institutions of Higher Learning, and the University of Engineering and Technology, Lahore under Faculty Development Programme (FDP) in collaboration with the Higher Education Commission (HEC) of Pakistan.

References

[1] J. Jellinek, Nanoalloys: tuning properties and characteristics through size and composition, Faraday Discussions, 138 (2008) 11-35.

[2] D. Stamatis, Z. Jiang, V.K. Hoffmann, M. Schoenitz, E.L. Dreizin, Fully Dense, Aluminum-Rich Al-CuO Nanocomposite Powders for Energetic Formulations, Combustion Science and Technology, 181 (2008) 97-116.

[3] M. Schoenitz, T.S. Ward, E.L. Dreizin, Fully dense nano-composite energetic powders prepared by arrested reactive milling, Proceedings of the Combustion Institute, 30 (2005) 2071-2078.

[4] M.M. Ba-Abbad, A.A.H. Kadhum, A. Bakar Mohamad, M.S. Takriff, K. Sopian, The effect of process parameters on the size of ZnO nanoparticles synthesized via the sol–gel technique, J Alloy Compd, 550 (2013) 63-70.

[5] C.H.-F. WEI Jian-Ning, GONG Chen-Li, ZHOU Zheng-Cun,, Grain Boundary Peak in a Foamed Zn-Al Eutectoid Alloy, Chin. Phys. Lett., 19 (2002) 381-384.

[6] C. Wagner, Z. Phys. Chem., B621 (1933) 25.

[7] N. Cabrera, N.F. Mott, Physics, 12 (1948) 163-184.

[8] N. Eisenreich, H. Fietzek, M. del Mar Juez-Lorenzo, V. Kolarik, A. Koleczko, V. Weiser, On the Mechanism of Low Temperature Oxidation for Aluminum Particles down to the Nano-Scale, Propellants, Explosives, Pyrotechnics, 29 (2004) 137-145.

[9] M.M.Y. Mench, C L | Kuo, K K, Propellant burning rate enhancement and thermal behavior of ultra-fine aluminum powders (Alex), Energetic materials - Production, processing

and characterization; Proceedings of the 29th International Annual Conference of ICT, Karlsruhe, Germany; GERMANY, 30-31 to 30-15.

[10] M.S. Aida, E. Tomasella, J. Cellier, M. Jacquet, N. Bouhssira, S. Abed, A. Mosbah, Annealing and oxidation mechanism of evaporated zinc thin films from zinc oxide powder, Thin Solid Films, 515 (2006) 1494-1499.

[11] M.A. Trunov, M. Schoenitz, X. Zhu, E.L. Dreizin, Effect of polymorphic phase transformations in Al2O3 film on oxidation kinetics of aluminum powders, Combustion and Flame, 140 (2005) 310-318.

[12] H. Delalu, J.R. Vignalou, M. Elkhatib, R. Metz, Kinetics and modeling of diffusion phenomena occurring during the complete oxidation of zinc powder: influence of granulometry, temperature and relative humidity of the oxidizing fluid, Solid State Sci, 2 (2000) 229-235.

[13] Z. Zhou, J. Liu, S. Hu, Studies on the kinetics process of tetra-needle-like ZnO whisker growth, J Cryst Growth, 276 (2005) 317-320.

[14] Y.I. Alivov, A.V. Chernykh, M.V. Chukichev, R.Y. Korotkov, Thin polycrystalline zinc oxide films obtained by oxidation of metallic zinc films, Thin Solid Films, 473 (2005) 241-246.

[15] X. Ma, M.R. Zachariah, Oxidation Anisotropy and Size-Dependent Reaction Kinetics of Zinc Nanocrystals, The Journal of Physical Chemistry C, 113 (2009) 14644-14650.

[16] M.S. Motta, P.K. Jena, E.A. Brocchi, I.G. Solórzano, Characterization of Cu–Al2O3 nano-scale composites synthesized by in situ reduction, Materials Science and Engineering: C, 15 (2001) 175-177.

[17] D.S. Wen, Nanofuels as an alternative energy carrier. Energy and Environmental Science, 3, 591-600

[18] K. Sullivan, G. Young, M.R. Zachariah, Enhanced reactivity of nano-B/Al/CuO MIC's, Combustion and Flame, 156 (2009) 8-8.

[19] J. Wang, A. Hu, J. Persic, J.Z. Wen, Y. Norman Zhou, Thermal stability and reaction properties of passivated Al/CuO nano-thermite, Journal of Physics and Chemistry of Solids, 72 (2011) 620-625.

[20] Y.F. Ivanov, M.N. Osmonoliev, V.S. Sedoi, V.A. Arkhipov, S.S. Bondarchuk, A.B. Vorozhtsov, A.G. Korotkikh, V.T. Kuznetsov, Productions of ultra-fine powders and their use in high energetic compositions, Propell Explos Pyrot, 28 (2003) 319-333.

[21] Kvartzkhava , Bondarenko V V, P.A.P.a.C.A. A, Oscillographic determination of the energy of electrical explosion of conductors, Zh. Eksp. Teor. Fiz. 1956, 31 745–51 (in Russian), (1956).
[22] F. Noor., E.P.B. Filho., A. Vorozhtsov., D. Wen., Thermal-Chemical Characteristics of Al-Cu Nano-Alloys, Sumbitted (2013).
[23] Y. Kotov, Electric Explosion of Wires as a Method for Preparation of Nanopowders, Journal of Nanoparticle Research, 5 (2003) 539-550.
[24] P. Song, D. Wen, Z.X. Guo, T. Korakianitis, Oxidation investigation of nickel nanoparticles, Phys Chem Chem Phys, 10 (2008) 5057-5065.
[25] F. Noor, H. Zhang, T. Korakianitis, D. Wen, Oxidation and ignition of aluminum nanomaterials, Phys Chem Chem Phys, 15 (2013) 20176-20188.
[26] Song P X and Wen D S* (2009) Experimental investigation of oxidation of tin nanoparticles. The Journal of Physical Chemistry C, 113 (31), pp 13470–13476
[27] J.E. Flinn, Particle size measurements: (4th edition), by Terence Allen; Chapman and Hall; 1990; pp. 832, Materials Science and Engineering: A, 161 (1993) 309.
[28] Y.H. Zhu, F.E. Goodwin, Microstructures of thermomechanically treated eutectoid Zn–Al alloy (II), J Mater Res, 10 (1995) 1927-1932.
[29] K.-L. Lin, L.-H. Wen, T.-P. Liu, The microstructures of the Sn-Zn-Al solder alloys, Journal of Elec Materi, 27 (1998) 97-105.
[30] W.R. Osório, C.M. Freire, A. Garcia, The effect of the dendritic microstructure on the corrosion resistance of Zn–Al alloys, J Alloy Compd, 397 (2005) 179-191.
[31] W.K. Tan, K.A. Razak, K. Ibrahim, Z. Lockman, Oxidation of etched Zn foil for the formation of ZnO nanostructure, Journal of Alloys and Compounds, 509 (2011) 6806-6811.
[32] A.P. Il'in, A.A. Gromov, G.V. Yablunovskii, Reactivity of Aluminum Powders, Combust Explos Shock Waves, 37 (2001) 418-422.
[33] A. Gromov, A. Ilyin, U. Förter-Barth, U. Teipel, Characterization of Aluminum Powders: II. Aluminum Nanopowders Passivated by Non-Inert Coatings, Propellants, Explosives, Pyrotechnics, 31 (2006) 401-409.
[34] S. Mey, Re-evaluation of the Al-Zn system, IInternational Journal of Materials Research, 84 (1993) 451-455.

List of Figures

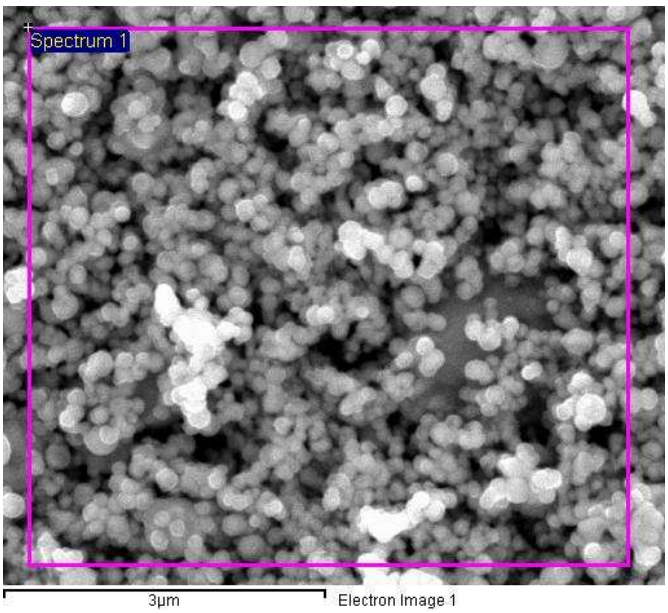

(a)

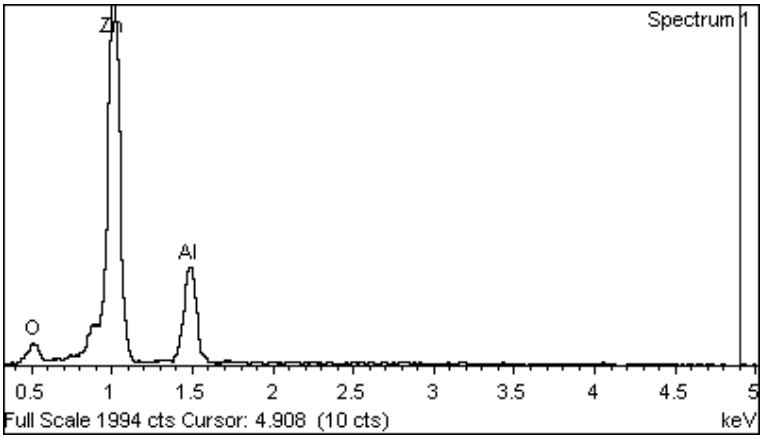

(b)

Fig. 1. (a) SEM micrograph showing the particles of nano alloy of Zn and Al are spherical and agglomerated; **(b**) EDS analysis of the sample showing a weak signal of Oxygen (before oxidation)

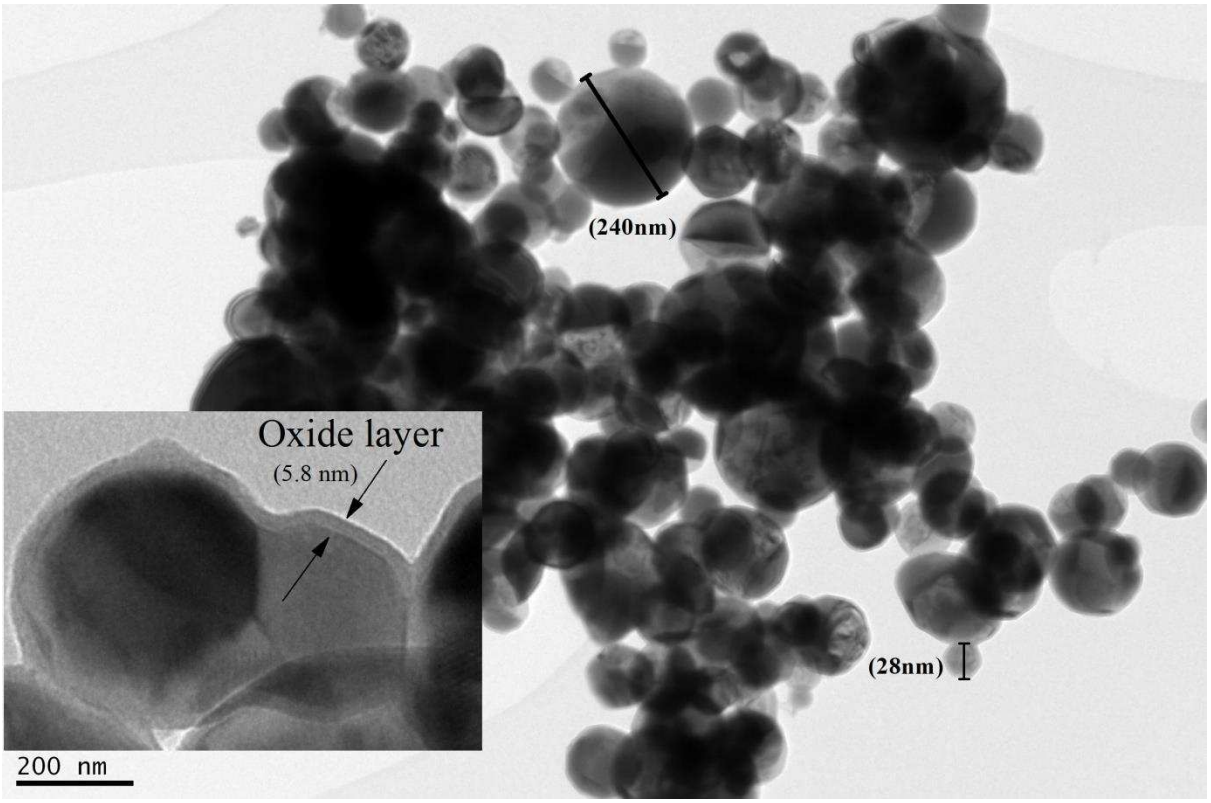

Fig. 2. TEM image showing that the particle diameter ranges from 28 to 240 nm and is encapsulated with an oxide layer of 5.8 nm thickness

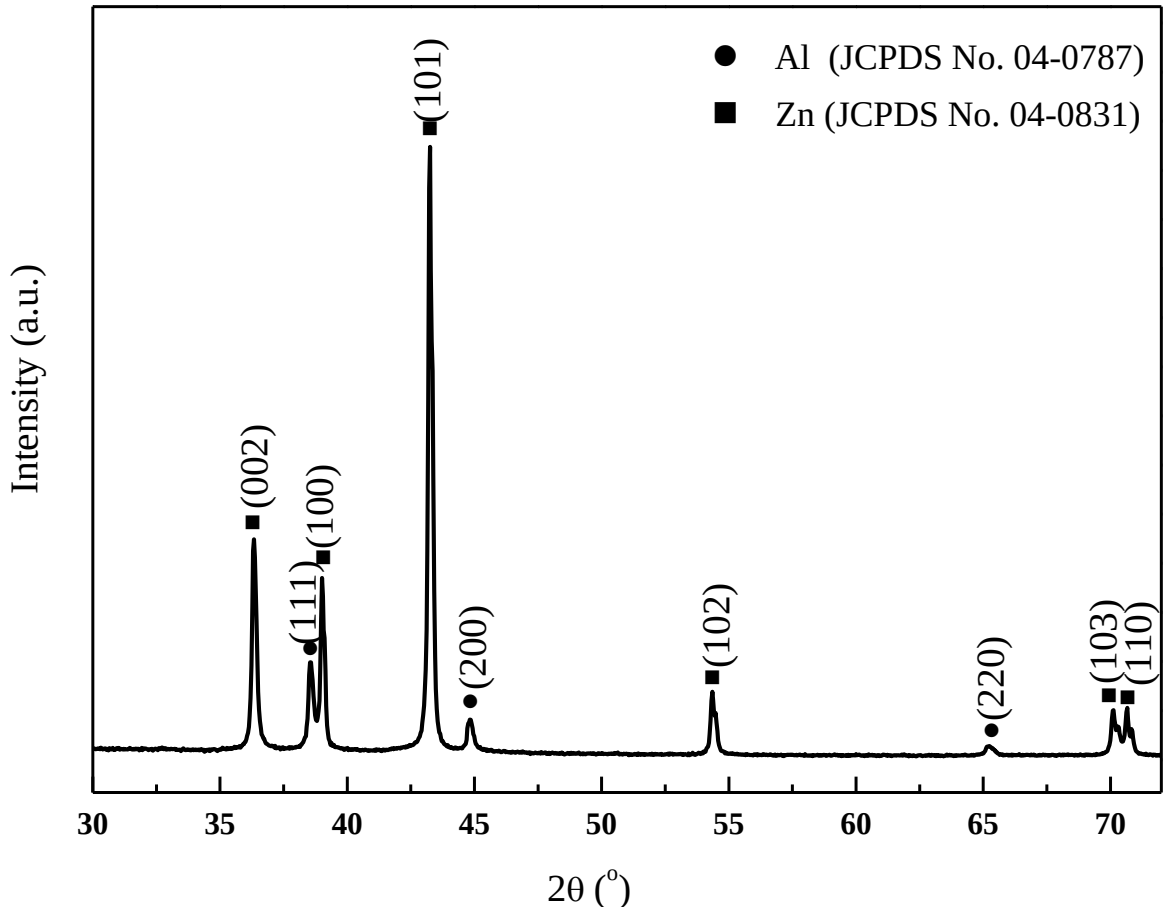

Fig. 3. XRD showing that the nano alloy of Zn and Al does not make intermetallic compounds

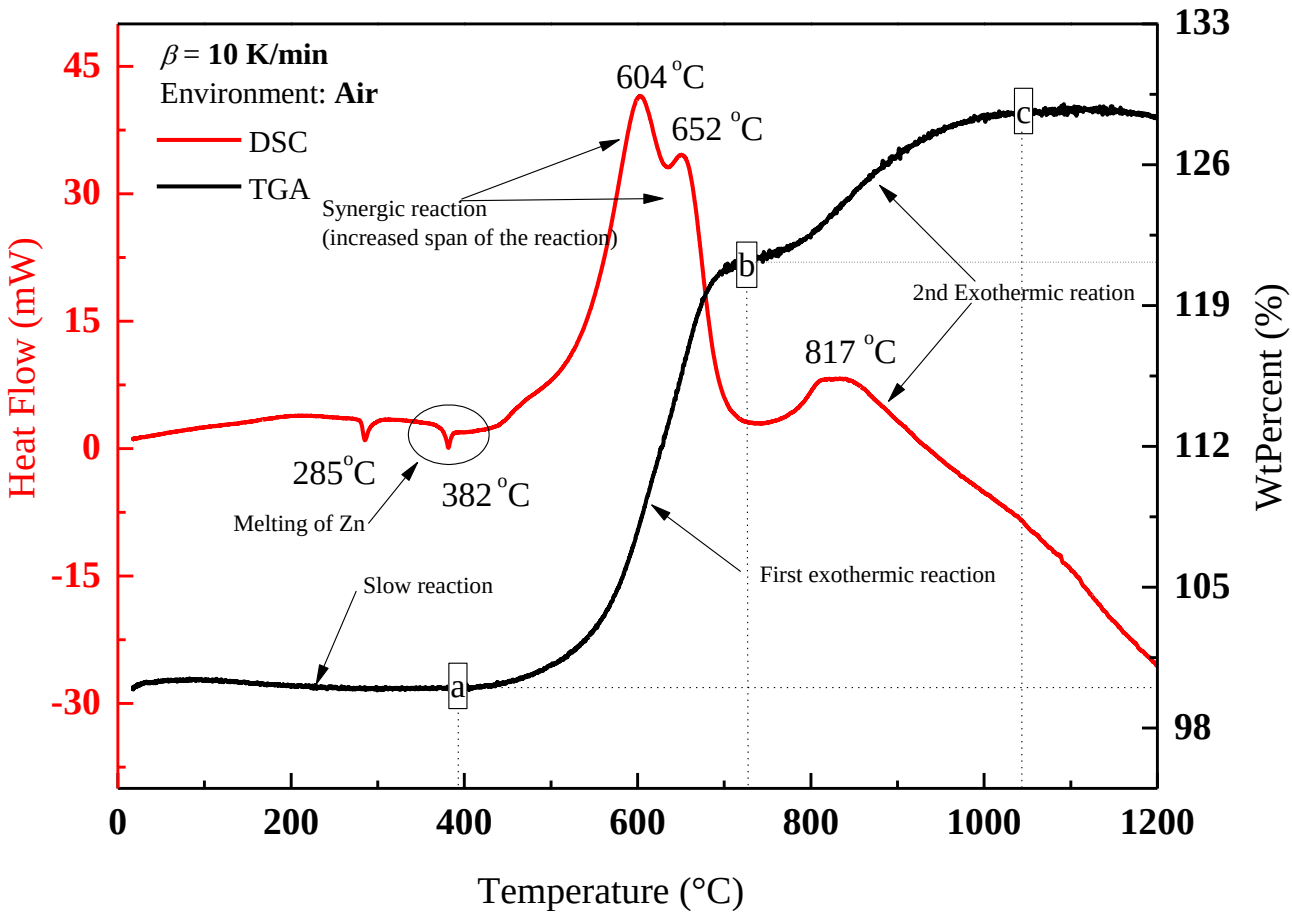

Fig. 4. DSC/TGA curve of nAlZn at a heating rate of 10 K/min (RT-1200°C) showing interesting features

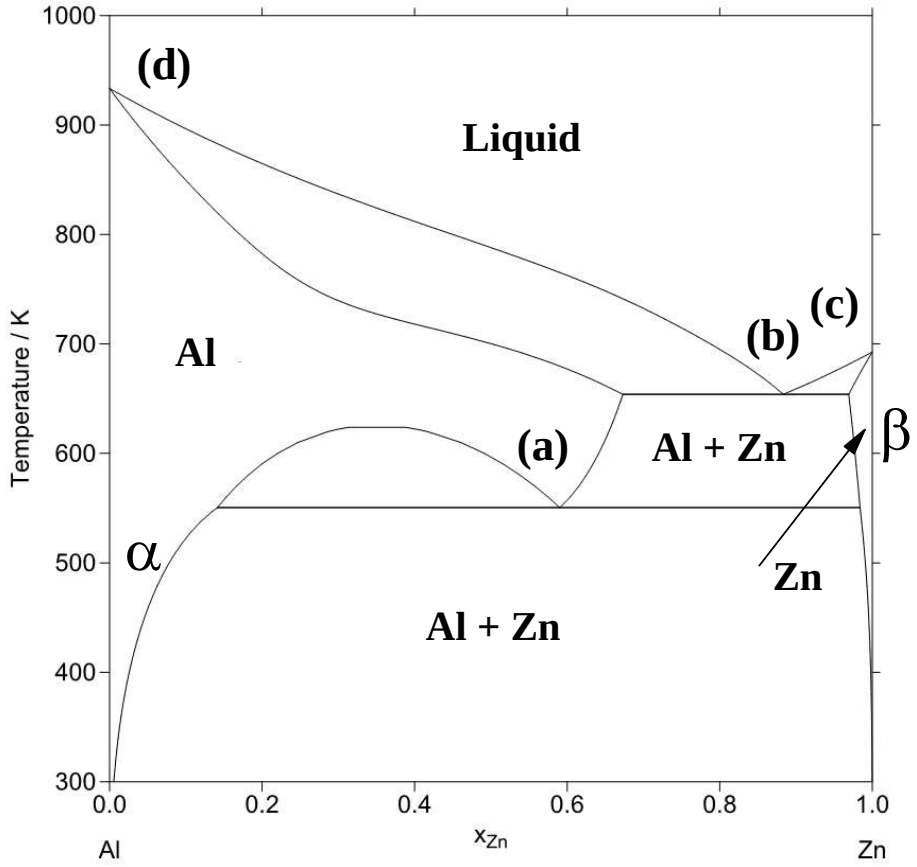

Fig. 5. Phase diagram of AlZn alloy showing different phases and important physical transformation temperatures [34]

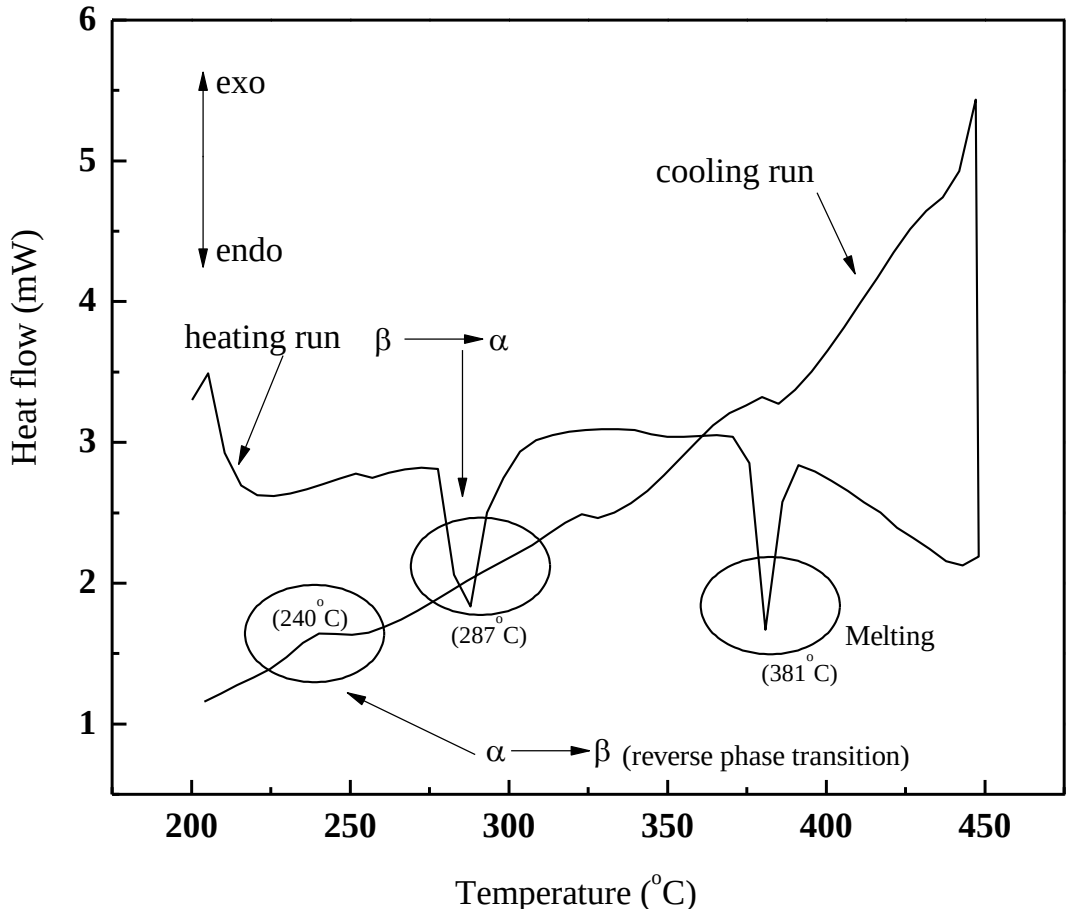

Fig. 6. DSC shows the endothermic transformation of β-phase to α-phase of nAlZn during the heating run and during the cooling run the sample goes through a reverse process and exhibiting a temperature hysteresis

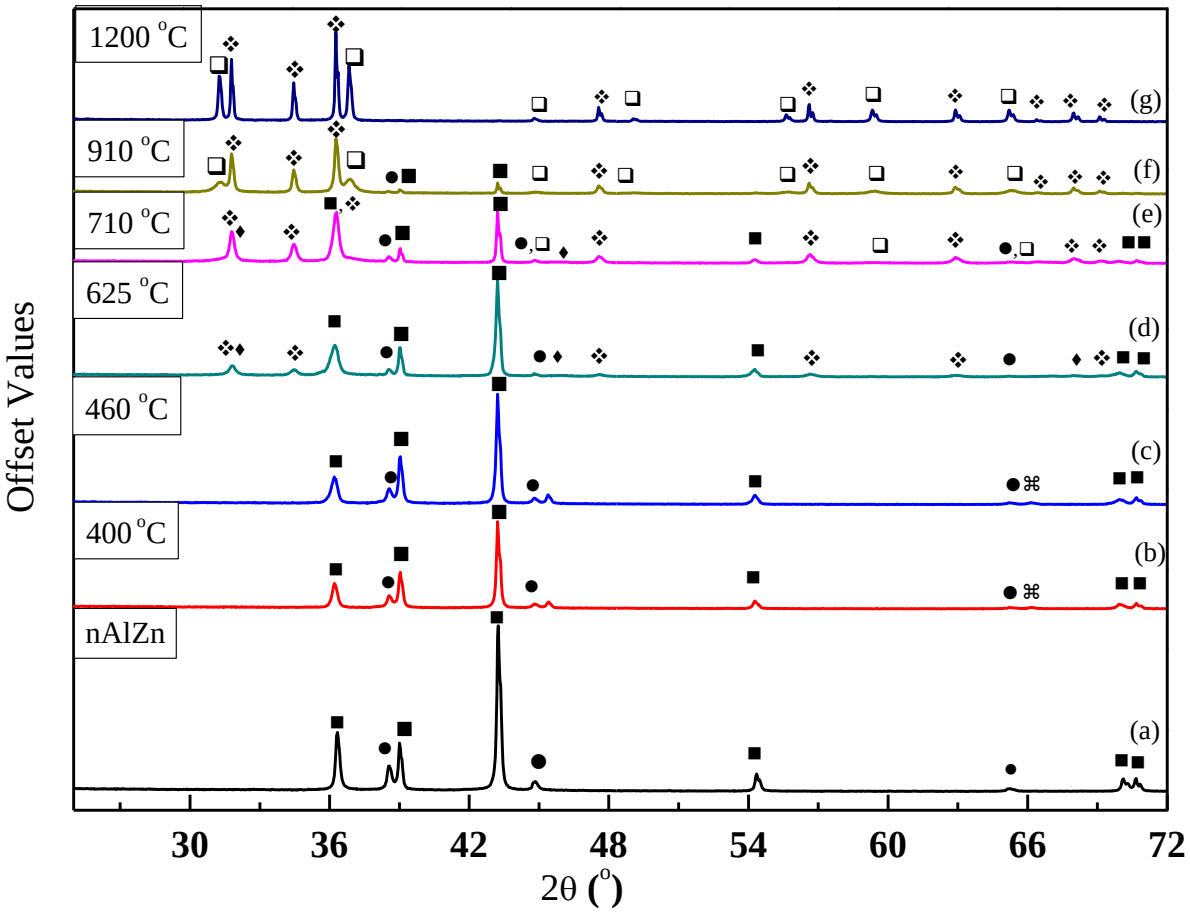

Fig. 7 (a-g). XRD peak patterns of the nAlZn at various temperatures at the heating rate of 10 K /min (● Al, ■ Zn, ❖ ZnO, ♦ γ-Al_2O_3, ❑ $ZnAl_2O_4$)

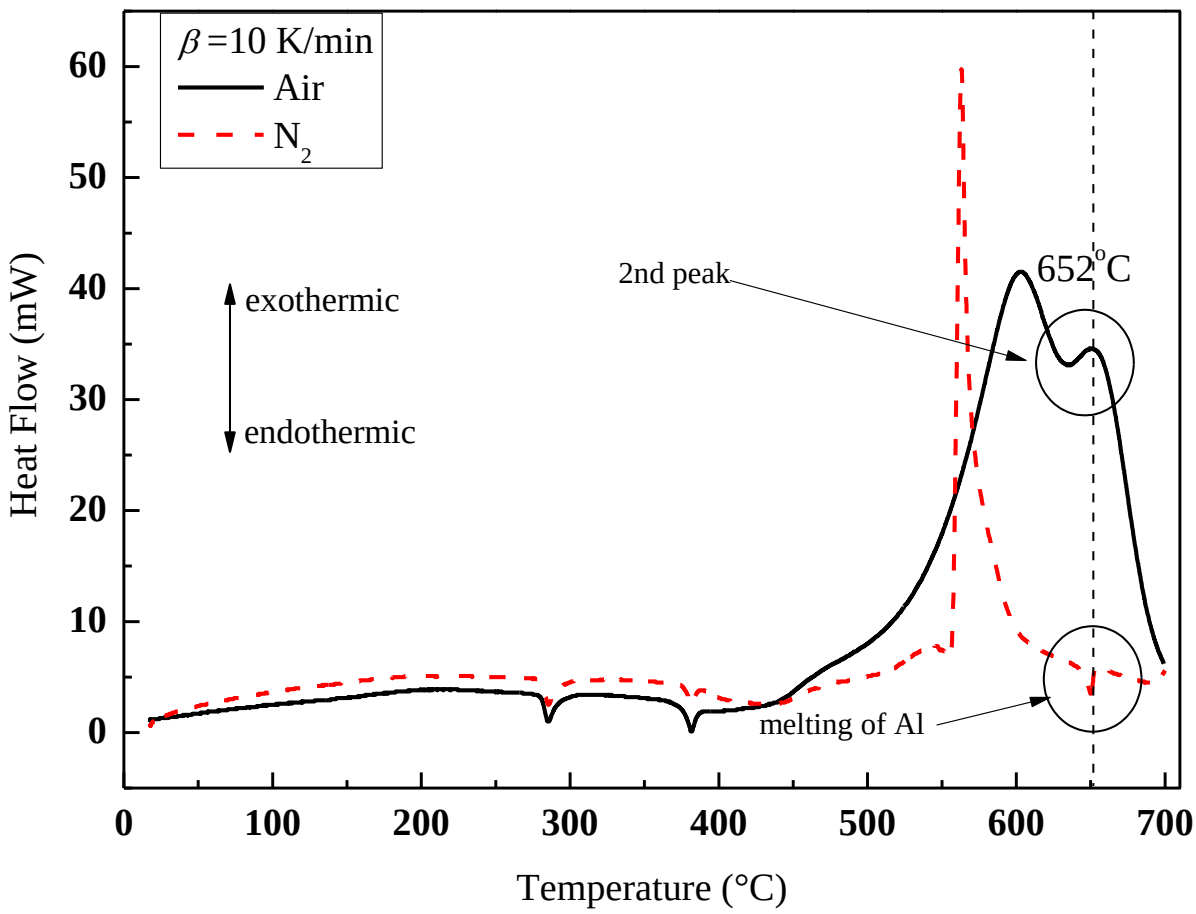

Fig. 8. DSC curve of the particles in air and nitrogen environments shows that the second oxidation peak in air coincides with the endothermic peak (melting of Al) in nitrogen

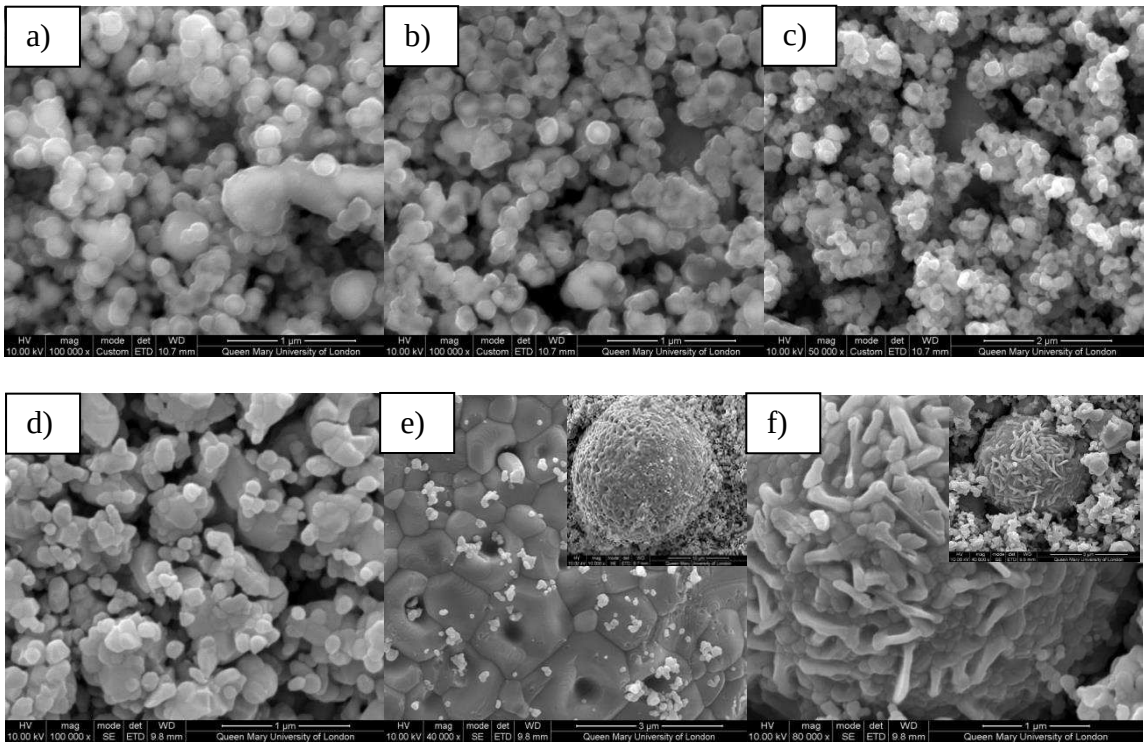

Fig. 9. SEM observations at (**a**) 625 ^{o}C (100 k); (**b**) 710 ^{o}C (100 k); **c**) 910 ^{o}C (50 k); (**d, e, f**) 1200 ^{o}C (100 k, 40 k, 80 k, respectively) at 10 K/min

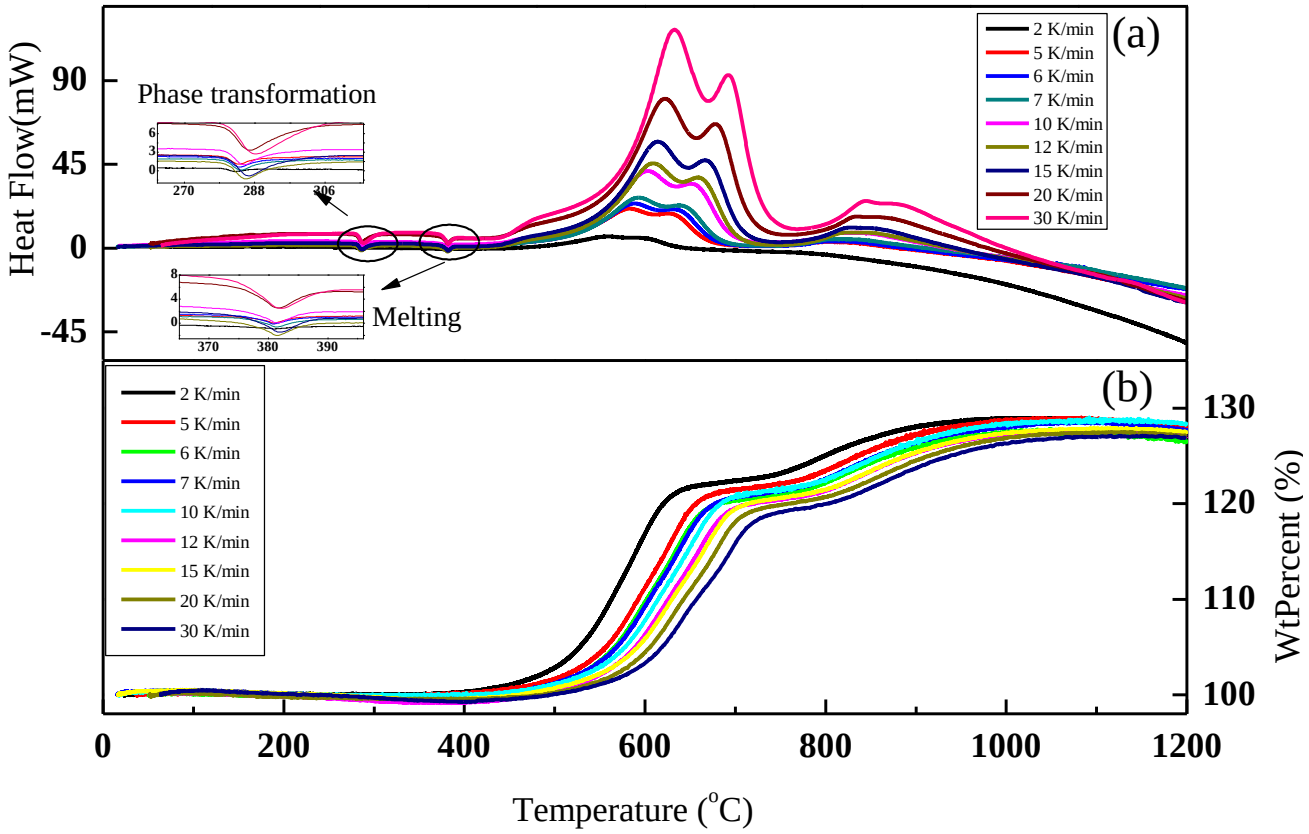

Fig. 10. (a) and **(b)** showing the DSC and TGA curves of the NA under heating rates of 2-30 K/min, respectively

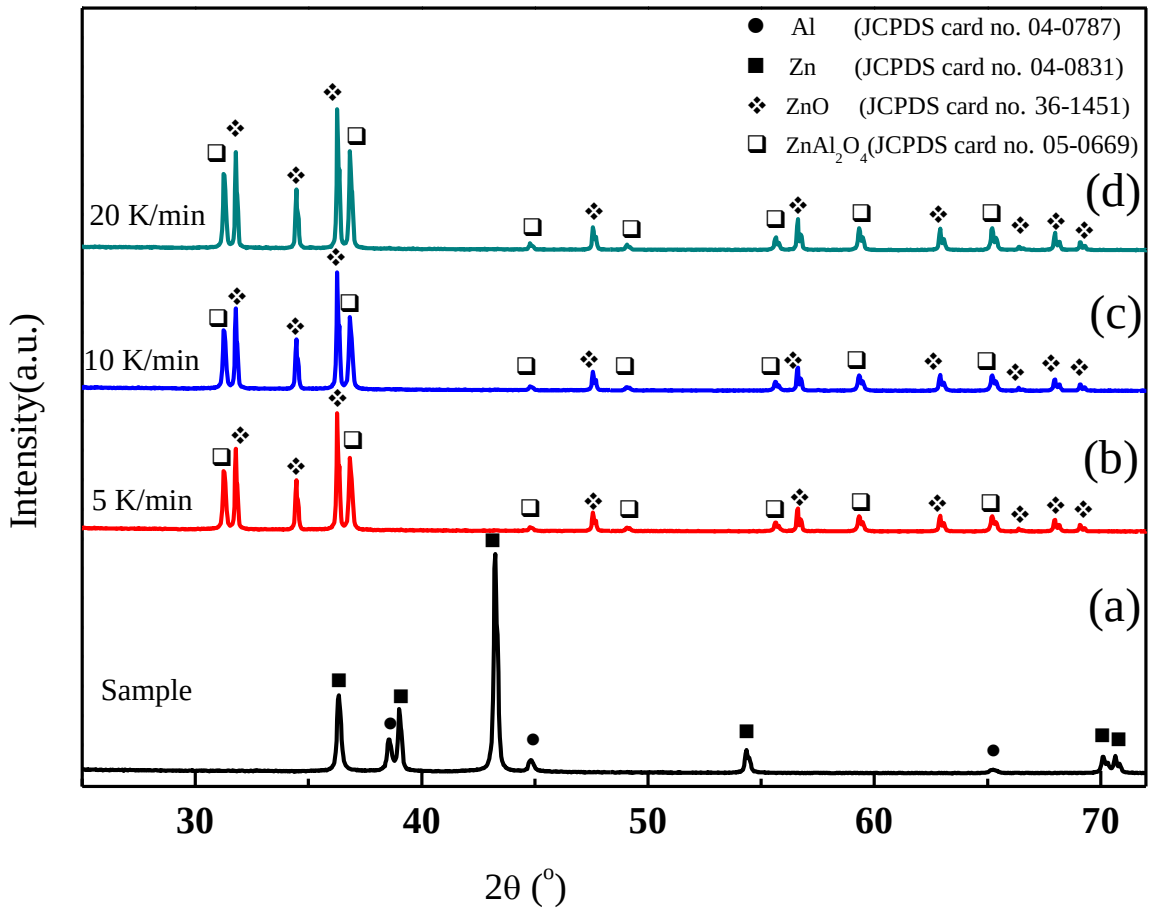

Fig. 11. XRD trace of nAlZn after oxidation under the heating rates of 5, 10 and 20 K/min

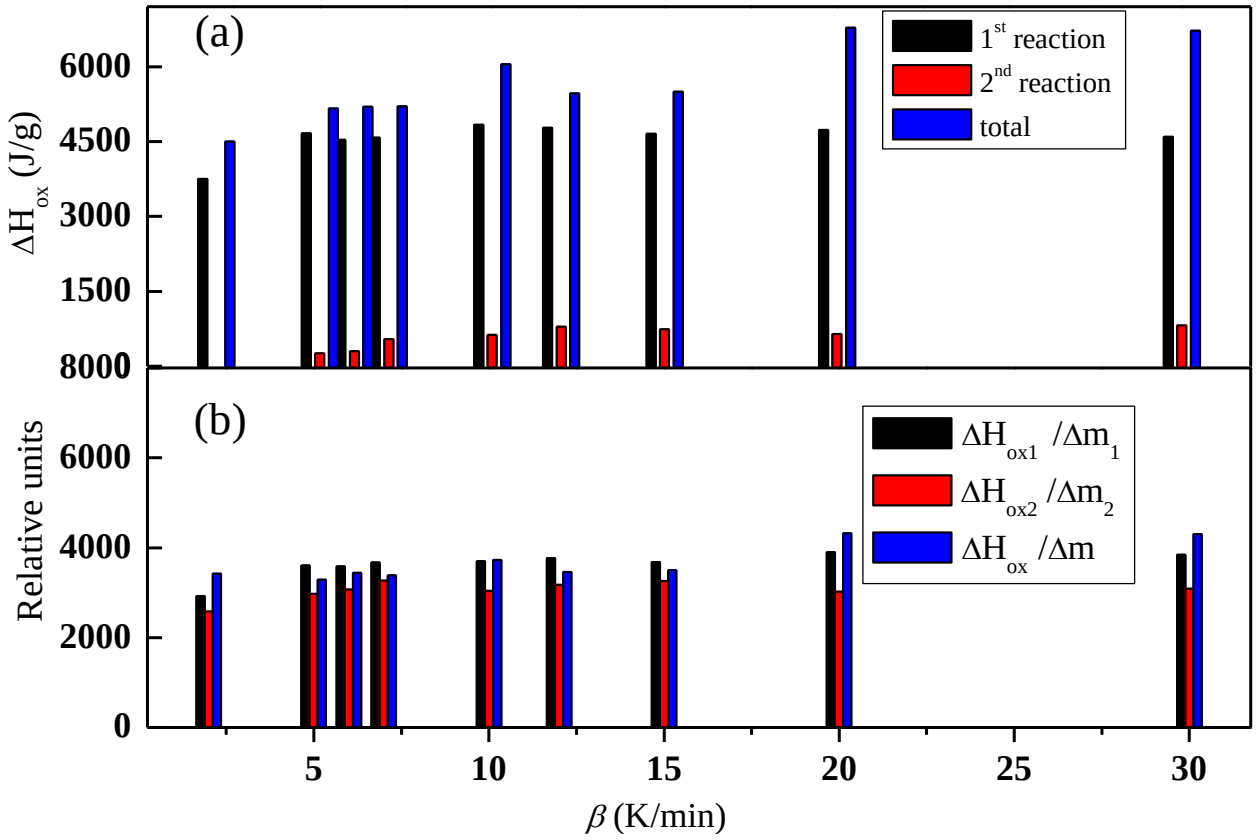

Fig. 12. (a) Heat produced during the two-step exothermic reactions; (**b)** the relative thermal effect (specific heat) of the nAlZn during oxidation at various heating rates

List of Tables

Table 1
Experimental Conditions

Sample	T_{f10}	β
	°C	K min^{-1}
nAlZn	400, 460, 625, 710, 910, 1200	2, 5-7, 10, 12, 15, 20, 30

Note:

T_{f10} is the termination temperature for DSC/TGA tests when β = 10 K min^{-1}

β is the heating rate

Table 2
EDS of nAlZn at various termination temperatures

Exp. conditions	O	Al	Zn	(Al+Zn)/O
Temperature	Weight	Weight	Weight	-
^{o}C	(%)	(%)	(%)	Ratio
25	4.82	18.26	76.92	19.75
460	5.75	18.54	75.71	16.40
625	20.19	17.33	62.48	3.95
710	24.32	14.26	61.42	3.11
910	24.62	16.41	58.97	3.06
1100	25.90	16.68	57.43	2.86

Table 3

Key features of the endothermic reactions

Heating rate	1st Endothermic Peak				2nd Endothermic Peak			
β	T_{pendo1}	T_{OS1}	$O.S_1$	ΔH_t	T_{pendo2}	T_{OS2}	$O.S_2$	ΔH_f
K/min	^oC	^oC	J/g/^oC	J/g	^oC	^oC	J/g/^oC	J/g
2	282	281	-0.43	7.7	381	379	-0.38	12.8
5	284	280	-0.44	17.8	381	378	-0.51	11.4
6	284	281	-0.53	17.1	381	378	-0.57	12.3
7	285	280	-0.53	18.3	381	378	-0.58	12.4
10	285	281	-0.64	19.7	382	377	-0.61	13.7
12	286	281	-0.71	19.0	381	377	-0.64	12.5
15	287	281	-0.72	20.9	382	377	-0.66	12.6
20	287	281	-0.84	19.5	382	377	-0.75	11.4
30	289	281	-0.92	22.6	382	375	-0.81	11.0
Mean±SD	**285.4±2.1**	**280.8±0.4**	**-0.6±0.2**	**18.1±4**	**381.4±0.5**	**377.3±1.1**	**-0.6±0.1**	**12.2±0.8**

Note:

T_{pendo1}, T_{pendo2}, are the peak values of temperatures of 1st and 2nd endothermic reactions; T_{OS1}, T_{OS2} are the corresponding onset temperatures and $O.S_1$, $O.S_2$ are the onset slops of the endothermic peaks.

ΔH_t , ΔH_f are the enthalpy of phase transformation and the enthalpy of fusion for eutectic melting of the NA

Table 4

Mass changed during the various steps of reactions.

β	Δm_{1a}	Δm_{1b}	Δm_1	Δm_2	Δm
K/min	%	%	%	%	%
2	12.4	9.2	21.6	-	29.07
5	12.6	8.6	21.2	3.7	29.37
6	12.5	8.3	20.9	3.9	28.6
7	13.1	7.9	21.0	4.8	29.2
10	13.1	8.3	21.4	5.5	29.15
12	13.0	8.0	21.1	6.0	28.61
15	13.1	7.8	20.9	5.8	28.52
20	12.1	8.2	20.3	6.4	28.01
30	12.2	7.9	20.1	6.4	27.91
Mean± SD	12.7 ± 0.4	8.2 ± 0.4	20.9 ± 0.4	5.3 ± 1.1	28.7 ± 0.5

Note:

Δm_1 is the mass changed during the first exothermic reaction

Δm_{1a} and Δm_{1b} are the mass changed during 2nd and 3rd substep of 1st exothemic reaction

Δm_2 is the mass changed during the second exothemic reaction

Δm is the final mass of the sample

Table 5

Key characteristics of the exothermic reactions on DSC curves

β	T_{pexo1}	h_{exo1}	T_{pe1}	h_{p1}	T_{pexo2}	h_{exo2}	T_{pe2}	h_{pe2}	T_{pexo3}	h_{exo3}
$Kmin^{-1}$	°C	mW	°C	mW	°C	mW	°C	mW	°C	mW
2	559	6.3	592.8	5.57	596	5.46	missing	missing	missing	missing
5	584	21.21	611	18.04	627	18.59	717	1.08	802	3.31
6	589	23.95	618	20.3	633	20.92	720	1.12	806	3.58
7	594	27.11	623	22.28	640	22.92	721	1.33	809	4.79
10	603	41.49	635.5	33.13	653	34.51	739	2.98	817	8.15
12	610	45.59	642	35.6	659	37.98	745	1.73	825	8.37
15	614	57.28	648	43.15	667	47.26	749	3.16	827	11.06
20	622	80.33	657	59.17	678	66.67	759	7.09	835	17.01
30	633	117.46	670	79.05	693	93.05	771	10.27	844	25.29
Mean	**600.9±22.4**	**46.7±34.4**	**633.1±24.2**	**35.1±22.7**	**649.6±29.3**	**38.6±27.2**	**740.1±19.6**	**3.6±3.3**	**820.7±14.7**	**10.2±7.6**

Note:

β is the heating rate, T_{pexo1}, h_{exo1}, T_{pexo2}, h_{exo2}, T_{pexo3}, and h_{exo3} are the temperatures and corresponding heat flow on DSC curve for the first second and third exothermic peaks respectively. T_{pe1}, h_{pe1}, T_{pe2}, h_{pe2}, are the temperatures and heat flow where the curves attain the first and second minima.

Table 6

Reactivity comparison of nAl and nAlZn under all heating rates

Reactivity Parameters / Samples	T_{on} °C	α %	T_{01} °C	ΔH/Δm a.u.
Al (211nm)	498.4±11.2	43.5±9.9	575.4±14.7	3994.7±418.7
nAlZn (141nm)	456.3±9.9	73.1±2.6	629.5±23.7	3649.1±393.6

Note:

Ton is the extrapolated onset temperature from TGA curve

α is the degree of conversion (up to 730 °C)

T_{01} is the temperature at which the maximum rate of oxidation is achieved on TGA curve

ΔH/Δm is the specific heat effect